

PAPER • OPEN ACCESS

A mechatronic leg replica to benchmark human–exoskeleton physical interactions

To cite this article: Miha Dežman *et al* 2023 *Bioinspir. Biomim.* **18** 036009

View the [article online](#) for updates and enhancements.

You may also like

- [Validation of the replica trick for simple models](#)
Takashi Shinzato
- [JavaFIRE: A Replica and File System for Grids](#)
Marko Petek, Diego da Silva Gomes, Claudio Fernando Resin Geyer et al.
- [The replica mean field theory for the glass matrix model](#)
Kazuo Nokura

Bioinspiration & Biomimetics



PAPER

OPEN ACCESS

RECEIVED
9 December 2022

REVISED
27 March 2023

ACCEPTED FOR PUBLICATION
17 April 2023

PUBLISHED
28 April 2023

Original Content from
this work may be used
under the terms of the
[Creative Commons
Attribution 4.0 licence](#).

Any further distribution
of this work must
maintain attribution to
the author(s) and the title
of the work, journal
citation and DOI.



A mechatronic leg replica to benchmark human-exoskeleton physical interactions

Miha Dežman^{1,10,*} , Stefano Massardi^{2,7,10,*} , David Pinto-Fernandez^{3,7} , Victor Grosu^{6,9} ,
Carlos Rodriguez-Guerrero⁸ , Jan Babič^{4,5,11} and Diego Torricelli^{7,11}

¹ Department of Automation, Biocybernetics and Robotics, Jožef Stefan Institute, Ljubljana, Slovenia

² Department of Industrial Mechanical Engineering (DIMI), University of Brescia (UNIBS), Brescia, Italy

³ Universidad Politécnica de Madrid, Madrid, Spain

⁴ Laboratory for Neuromechanics and Biorobotics, Jožef Stefan Institute, Ljubljana, Slovenia

⁵ Faculty of Electrical Engineering, University of Ljubljana, Ljubljana, Slovenia

⁶ Department of Mechanical Engineering, Robotics & Multibody Mechanics Research Group (R&MM), and Flanders Make, Vrije Universiteit Brussel, Brussel, Belgium

⁷ Instituto Cajal, Spanish National Research Council (CSIC), Madrid, Spain

⁸ Department of Mechanical Engineering, KU Leuven, Leuven, Belgium

⁹ Research and Development Department, GROVIXON BV, Vilvoorde, Belgium

¹⁰ These authors have contributed equally to this work.

¹¹ These authors have contributed equally to this work share senior authorship.

* Authors to whom any correspondence should be addressed.

E-mail: miha.dezman@kit.edu and stefano.massardi@cajal.csic.es

Keywords: exoskeleton evaluation, wearable robot, exoskeleton benchmark, interaction forces, leg replica, sensorized dummy, pHEI

Abstract

Evaluating human-exoskeleton interaction typically requires experiments with human subjects, which raises safety issues and entails time-consuming testing procedures. This paper presents a mechatronic replica of a human leg, which was designed to quantify physical interaction dynamics between exoskeletons and human limbs without the need for human testing. In the first part of this work, we present the mechanical, electronic, sensory system and software solutions integrated in our leg replica prototype. In the second part, we used the leg replica to test its interaction with two types of commercially available wearable devices, i.e. an active full leg exoskeleton and a passive knee orthosis. We ran basic test examples to demonstrate the functioning and benchmarking potential of the leg replica to assess the effects of joint misalignments on force transmission. The integrated force sensors embedded in the leg replica detected higher interaction forces in the misaligned scenario in comparison to the aligned one, in both active and passive modalities. The small standard deviation of force measurements across cycles demonstrates the potential of the leg replica as a standard test method for reproducible studies of human-exoskeleton physical interaction.

1. Introduction

Exoskeletons are wearable robots that assist the movements and/or increase the motor capabilities of individuals by means of forces applied to body limbs through physical connection interfaces. Currently, the use of robotic exoskeletons is highly extended in multiple fields [1] such as: (i) medical, used as a tool to mobilize affected limbs during rehabilitation therapies [2], (ii) personal assistance, with the aim of supporting the motion of people with mobility problems [3], (iii) industrial, used for improving ergonomics and reducing the worker injuries during

repetitive tasks [4, 5], and (iv) military, with the goal of increasing the physical capabilities of humans [6]. The demand for exoskeletons continues to increase every year, due to the aging of society, the increase in the incidence of neurological injuries, such as stroke, and the increase in mobility deficiencies among the population [7]. However, the benefits of this new generation of devices are limited by how efficiently and safely they can transmit power through coupling forces to the user's biological structures [8].

This force exchange must be coordinated and reciprocally adapted to maximize the achievement of the functional goal and, at the same time, minimize

adverse events resulting from unexpected behaviors of the actuators. Growing evidence indicates that inefficient device-to-human power transmission is a critical problem for wearable assistive devices [1], which undermines potential health and performance benefits. Up to 50 per cent of the mechanical power may be lost in the interaction due to soft tissue compression and harness compliance [9]. Power transmission issues are related to several factors such as kinematic compatibility, resulting in joint misalignments, and interface design, which affects contact stiffness and relative motion between the limb and the robot [8, 10]. Despite a recent growth of studies focusing on physical human–exoskeleton interaction (pHEI), the transmission of forces due to the physical coupling has not been investigated in a systematic way so far [11]. One of the reasons for this is the difficulty to directly and quantitatively measure the dynamics of force transmission as well as their effects on comfort and pain. For example, discomfort may originate from a combination of pressure points, device migration (relative displacement) and abnormal internal joint forces [12, 13]. Force mapping shows that the force is not evenly distributed over the interface surface area [14, 15]. During some exercises, it may happen that only the interface edge is in contact with the user, generating a concentration of the force over a smaller area, increasing pressure [14]. Literature shows that research studies on efficient transmission of power to a user through interfaces are still limited [11].

Additionally, exoskeletons represent a particular technology in which regulation and standards are not yet addressed in a systematic way [16, 17]. Considering the importance of human–exoskeleton contact issues, the definition of protocols and methods for their contact characterization is becoming a pressing requirement for their safety assessment. In a recent survey [18], more than half of the safety skills considered as essential requirements for rehabilitation robots were related to physical interaction. New efforts are required to assess, characterize and define pHEI in a more systematic and harmonized way.

In this work, we present a mechatronic replica of a human leg, composed of a human-like actuation system at the knee level and an anthropomorphic sensorized surface able to assess interaction forces in three dimensions. The proposed prototype enables the execution of reproducible experiments (especially in the field of rehabilitation exoskeletons) to quantify the abilities of an exoskeleton for safe interaction with a user. The proposed testbed aims to minimize the amount of testing required with human participants by promoting the use of the leg replica until the system is sufficiently safe.

The paper is organized as follows: section 2 provides a brief description of previous scientific works related to this topic. Section 3 provides the requirements for the design of the leg replica and

a detailed description of the underlying hardware and software components and solutions. Section 4 describes the setup and experimental protocols used to evaluate the proposed leg replica, whose results are presented in section 5. The paper ends with a discussion in section 6 and a conclusion in section 7.

2. Related work

Our work is motivated by the necessity of benchmarking pHEI while minimizing the risks for human participants. The use of dummies represents a promising approach with the possibility to fit in safety assessment plans to emulate the interaction between a human and the machine, reducing the user exposure to adverse events and increasing the intensity and variability of tests [19]. Mannequins or dummies have been employed to investigate skin effects, off-axis joint rotation effects, and other areas where fatigue or unsafe conditions impeded the tests with humans [20]. A realistic dummy able to reproduce human-like movements at different body joints and functional tasks would be highly beneficial in the field. Unfortunately, active test dummies for exoskeletons are still not present in the market. Literature review shows only a few instances where dummy limbs are used in evaluations of assistive wearable devices. Mannequin's limbs were purely used as wearing devices for both upper [21] and lower [22] limb exoskeletons. Dummy limbs were chosen prior to human tests in exoskeletons experimental validations either using a simple mannequin lower leg [23] or a complex dummy arm from 3D human scanning [24]. Human dummy models have been proposed to improve the human–exoskeleton fitting [25]. An advanced dummy test case was presented in [26], in which a full-body humanoid robot [27] was used to prove the humanoid control performance while wearing an assistive device. Another study used a lower-leg dummy for the safety assessment of a wearable robot, focused on evaluating the effects of a misaligned knee joint [28]. Force sensors were placed on the robot to be tested rather than on the passive dummy. The proposed dummy also had an extension mechanism that mimics the lower leg cuff's motion during leg extensions. A remarkable work in this direction was conducted in [29], where for the first time a passive dummy leg was equipped with a torque sensor in the knee joint, whose readings were systematically related to joint misalignments. Most of the existing approaches were based on passive test dummies without any contact measurements. Direct force measurements are usually obtained from load cells placed at the contact points or in customized cuffs [30–33], force-sensing resistors (FSRs) [34, 35] (which are also to extract normal pressures [15, 36]), and optical sensors [37, 38]. These approaches present two general difficulties. The first is to achieve a correct placement of sensors

at the contact point between the device and the user. The second is related to the correct and reliable measurement of shear forces. For these reasons, introducing a network of sensors able to measure the force transmission in a reliable and precise way is crucial. Additionally, a dummy with an intrinsic measure of interaction forces (including shear components) and independence from the tested devices would be highly advantageous. Attaching a wearable device to such a dummy would not require any additional attachment components beyond the exoskeletons straps, solving the issues related to space and quality of the measurements and leaving the device interfaces free to move close to real-life operating conditions.

3. Materials and methods

3.1. Requirements for the leg replica

The main goal of the leg replica is to closely mimic human-like joint dynamics. Mimicking dynamics means that the proposed leg replica should feature weight, inertia and actuation properties comparable to those of a human leg. These properties are split into *anthropometric* and *mechanical* design requirements. The *anthropometric* requirements reflect properties such as dimensions, inertia, external shape, mass, degrees of freedom (DoF) and ranges of motion (RoM). The *mechanical design* requirements include the integration of sensors and actuators in the device. The goals that shape anthropometric requirements are summarized as follows:

- Reaching comparable leg dimensions to a human leg and an external surface shape comparable to human 3D surface scans.
- Reaching leg segment mass and mass center location comparable to those of a human leg [39].
- Reaching a comparable RoM between passive and active DoFs [40].

Anthropometric dimensions of the reference human leg are based on data from [39, 41]. The limb lengths of interest are depicted in figure 1(a) and the corresponding values are collected in table 1.

3D surface scans (figure 1(b)) were combined with a computed tomography (CT) scan (figure 1(c)) in one CAD model. The external shape of the CAD leg was designed to follow their shape as much as possible. Figures 1(b)–(d) depicts the design process. The freely available CT scan data comes from the online tool democratiz3D® and features a 3D-reconstructed lower body model including skin, muscle tissue and bones. The 3D surface scans of the leg were supplied by Vrije Universiteit Brussel (VUB). All 3D scans and CT scan reconstructions were scaled to reach a hip joint height of approximately 90.1 cm, i.e. the *Popliteal height* from table 1. The location of joint axes were determined with the reconstructed 3D bone model as shown in figure 1(b). All the 3D surface

models are superimposed acting as a blueprint to model the final parametric surface model of the leg (figure 1(c)). The final leg model is a solid parametric CAD model, which allows manual adjustments to its shape even in later design stages. The adjustments to the shape model are automatically reflected in the final solid CAD model, which was used as a reference for all other leg components that needed to follow the shape of the external leg.

The data on the masses of different leg segments and the corresponding mass center locations are adopted from [39] and collected in table 2. The average mass of the *Thigh* segment is **6.0(1.2) kg**, resulting from the average of the *Left Thigh* and *Right Thigh* segments, as shown in table 2. Similarly, the average mass of the *Calf+Foot* segment is **3.7(0.7) kg**. Both values were used in this work as design targets and evaluation criteria. Clauser's book also provides the relative distances to the respective mass centers. These are gathered in table 3. Accordingly, the mass center of the *Thigh* segment lies at a distance of **45.1(4.4)%** from the hip towards the knee joint. The mass center of the lower leg (*Calf+Foot*) lies at a distance of **51.3(3.5)%** from the knee joint to the heel. Finally, the range of motion data of a human leg was taken from [40] and collected in table 4. The leg design matches these values as much as possible.

The *mechanical design* requirements stem from the requirements of different mechanical components, including the actuator, the force sensors and other electronic components. This also includes the custom-made aluminum structure that supports the whole leg. The requirements are summarized as:

- Aluminum structure representing the leg replica's bones with attachment features and strength to support the nominal loads of the actuation unit [42].
- Integration of eight K3D60a load cells under each surface shell (ME-Meßsysteme GmbH).
- External shells attached to these sensors to transmit externally perceived loads on the leg replica's surface to the respective force sensors placed below the shell.
- Integration of the required PCB electronic circuits in the available internal space of the leg, without affecting RoMs and external shape.

The leg's internal structure is discussed further in section 3.3.

3.2. Knee actuation

This section briefly describes the actuation solution used to drive the knee joint of the leg replica. The knee joint is the only active joint of the leg replica and is actuated by a SMARCOS actuator unit [42]. SMARCOS is a mechanically compliant actuator with manually adjustable compliance based on the MACCEPA mechanism, developed by VUB [43].

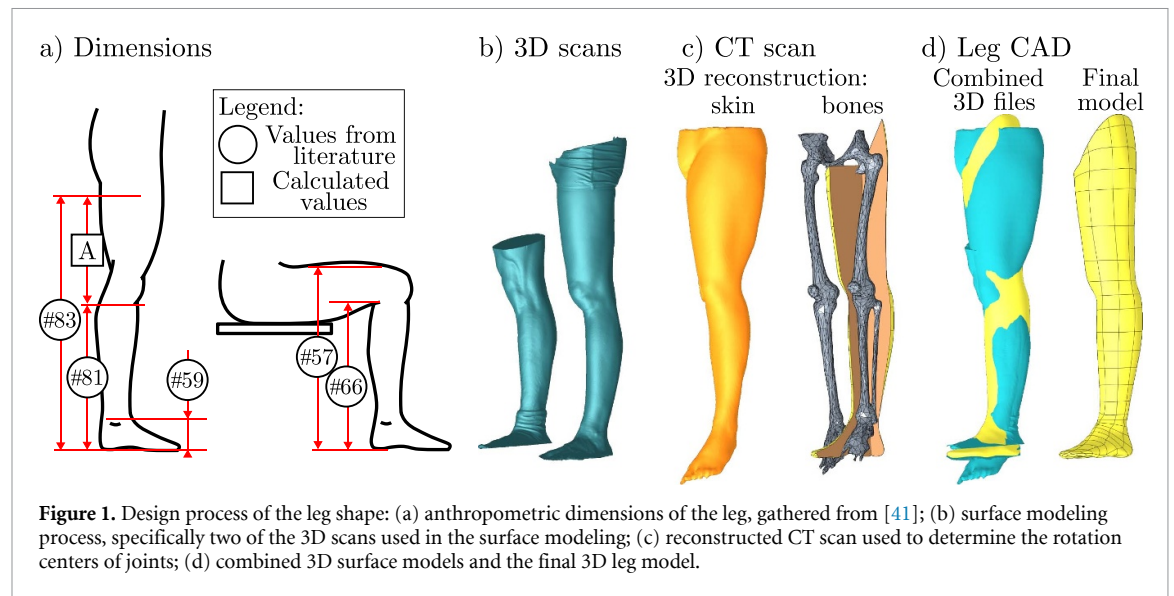


Table 1. Leg anthropometric dimensions.

# ^a	Dimension name	Mean (cm)	SD (cm)	Var (cm ²)
57	Knee height, sitting	55.4	2.8	7.8
59	Lateral malleolus height	7.3	0.6	0.3
66	Popliteal height	43.0	2.5	6.2
81	Tibial height	46.8	2.7	7.1
83	Trochanterion height	90.1	4.9	24.2
A ^b	Thigh length (#83 - #81)	43.3 ^c	5.6 ^c	31.3

Data from this table is adopted from [41] and correspond to dimensions of a 50th percentile male.

^a These values correspond to figure 1(a) and correspond to measurement numbering in [41].

^b A is calculated as a difference between measurement #83 and #81.

^c The mean and SD values based on #83 and #81 are calculated as

$E(A \pm B) = E(A) \pm E(B)$; $Var(A \pm B) = Var(A) + Var(B)$. The values are deemed independent.

Table 2. Mass of human leg segments^a.

Body part	Mass ^b (kg)														AVG (kg)	SD (kg)
R. Thigh	7.17	5.95	7.65	6.69	6.15	4.86	3.39	6.12	5.37	4.77	7.16	6.90	7.22	4.66	6.00	1.18
L. Thigh		5.83	7.30	6.22	6.75	4.81	3.50	6.48	5.52	5.29	7.09	6.26	7.70	5.14		
R. Calf+Foot	3.97	3.23	4.47	3.95	3.93	2.98	2.61	3.47	2.91	2.88	4.83	4.77	3.96	3.32	3.65	0.72
L. Calf+Foot		3.24	4.50	3.98	3.90	2.80	2.60	3.38	2.84	3.04	4.85	4.81	4.05	3.43		

^a Data is adopted from [39].

^b These are the weights of specific body segments of different individuals.

Table 3. Mass center locations^a.

Body part		%L ^b (%)						AVG (%)	SD (%)
R. Thigh	46.8	43.0	43.2	46.9	42.5	43.8	43.3	45.1	4.4
L. Thigh		57.0	44.6	47.6	38.8	43.4			
R. Calf+Foot			50.0	53.1	52.1	56.4	43.4	51.3	3.5
L. Calf+Foot			51.7	51.4	53.1	50.8			

^a Data is adopted from [39].

^b Center of mass location as percentage of the proximal end or joint axis and the total segment length. Thigh length is measured from hip joint to knee joint. Calf+Foot is measured from the knee joint to the heel.

It features different properties of human joints such as: (1) allowing energy absorption from external interactions, (2) being highly backdrivable, and (3) allowing high-resolution torque control. Figure 2

shows its main components. It includes a 70 W brush-less motor (Maxon Motor EC-i 40) combined with a ball-screw transmission (Maxon spindle drive GP32S 1:1) and an integrated spring with a stiffness of

Table 4. Human leg range of motion^a.

Joint	Movement	RoM (deg/deg)
Ankle	inversion/eversion	30/20
	plantarflexion/dorsiflexion	65/25
	adduction/abduction	45/50
Knee	flexion/extension	(135–150 ^b)/0
	adduction/abduction	25/40
Hip	flexion/extension	(80–120 ^b)/20
	internal/external rotation	35/45

^a Data is adopted from [40].

^b The maximum flexion is represented as a range between two values.

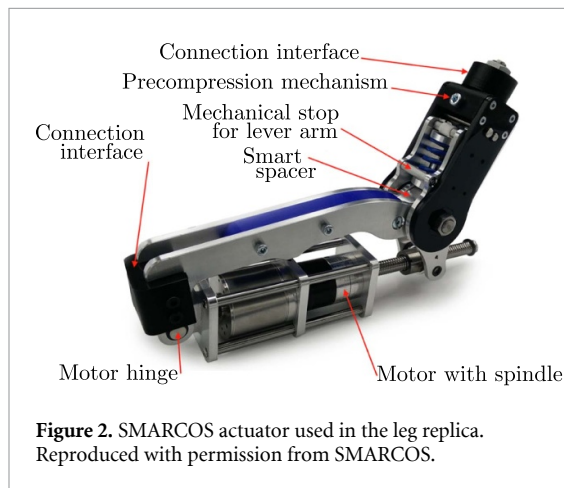


Figure 2. SMARCOS actuator used in the leg replica. Reproduced with permission from SMARCOS.

118.2 N mm⁻¹. The unit is backdrivable despite the use of a ball screw transmission, thereby allowing high resolution torque control and state-of-the-art transparency. Both ends of the actuator include connection interfaces, which are exploited to connect both the upper and lower leg replica segments. Its electronics is based on a custom developed control unit that implements the EtherCAT communication protocol and interfaces with an ESCON 50-5 motor controller (maxon motor AG). It also features its own strain gauge-based torque sensor and an incremental encoder. Additionally, several analog to digital converters and digital inputs and outputs are also available for the end-user application.

3.3. Mechanical design and sensors

This section describes the mechanical design of the leg replica and its main components. Both the prototype and a depiction of its kinematics are shown in figure 3.

The three joints of the prototype were simplified in comparison with real human joints in order to reduce their mechanical complexity. The hip and ankle joints were simplified to a ball joint and allow passive rotation in three DoFs. The knee joint was simplified to a 1-DoF joint. Note that while such simplifications are common in the literature, the kinematic behavior of human joints is complex [40],

featuring not only pure rotations, but also movable rotation centers and rolling contact motions. Design of a knee joint that would more closely follow the behavior of real human joints would require a redesign of the SMARCOS unit and was therefore not realized at this stage.

An aluminum structure forms the core of the leg replica and includes many design solutions for the attachment of sensors, electronics and the actuator unit. It is shown together with its main components in figure 4. In addition, figure 5(d) shows the disassembled prototype.

The aluminum structure was divided into smaller sub-components that were screwed together. As the leg replica is an experimental prototype, this design strategy allows for later modifications to the internal structure if required. The upper leg structure attaches to the hip joint, whereas the lower leg structure attaches to the foot. A fixing element (the blue 'hip mounting fixture' in figure 4(a)) allows the leg replica to be mounted on a commercially available aluminum profile. In addition, the fixture component is connected to the passive ball joint of the hip. The ball joint assembly is shown in figures 5(a) and (b). By means of fastening screws, passive sliding movements or rigid fixation can be performed at the hip. If passive hip movement is required, the screws can be unscrewed slightly to allow sliding movement. If rigid fixation of the joint is required, the screws can be tightened to increase the forces on the ball joint. The ball joint at the foot uses the same screw fixation principle as the hip joint, as shown in figure 4(a). Depending on the need, the foot also allows passive movement or rigid fixation by fastening of the screws.

The leg replica is divided into eight surface sections, or *surface shells*, as shown in figure 4(c). A triaxial load cell is located beneath each shell (DIM. 60 mm × 60 mm × 25 mm, from ME-Meßsysteme, GmbH). Its location is relatively close to the center of each surface shell. Four surface shells belong to the upper leg and four to the lower leg.

This arrangement was chosen to ensure that two force sensors are placed at each strap position of a typical full leg exoskeleton featuring four attachment

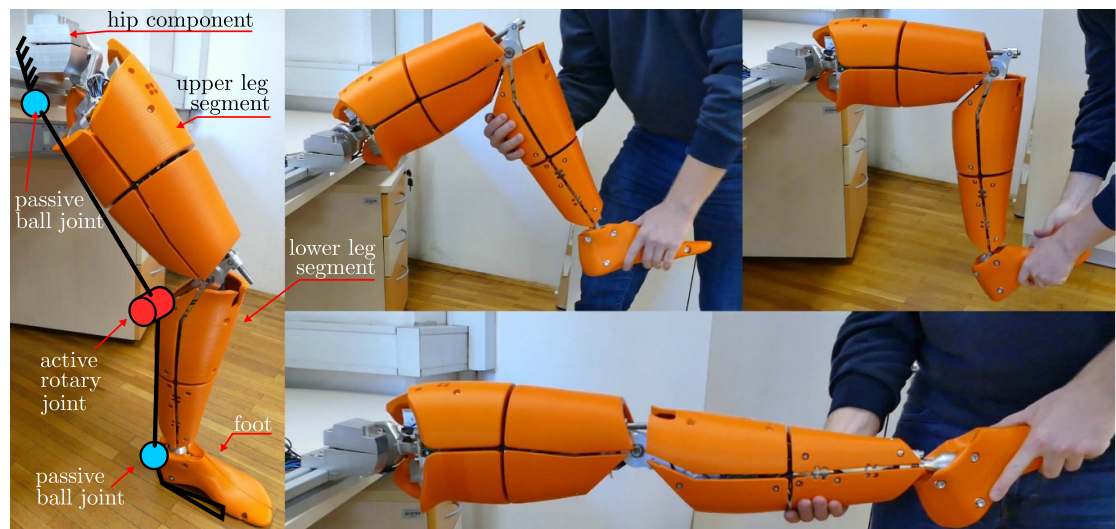


Figure 3. Different views of the leg replica prototype, combined with its kinematic structure. The leg includes two passive ball joints each with 3 DoFs (blue color) and one active rotary 1-DoF joint (red color) at the knee.

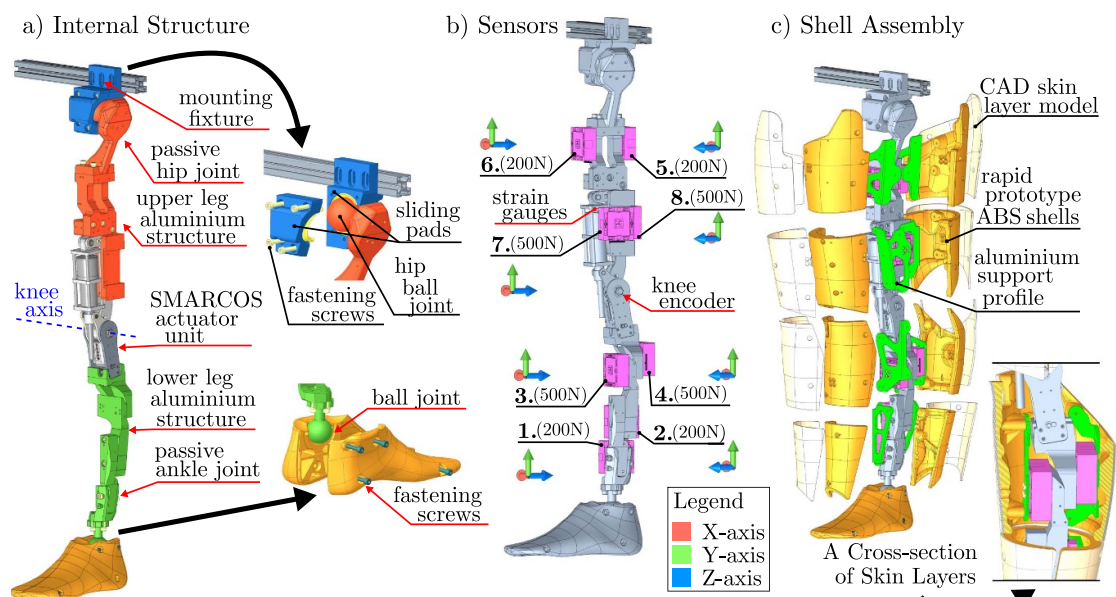


Figure 4. Leg replica's main components: (a) leg's internal structure, (b) force sensor locations, (c) shell assembly layout across the leg surface. Note that (b) shows each load cell's number and coordinate system.

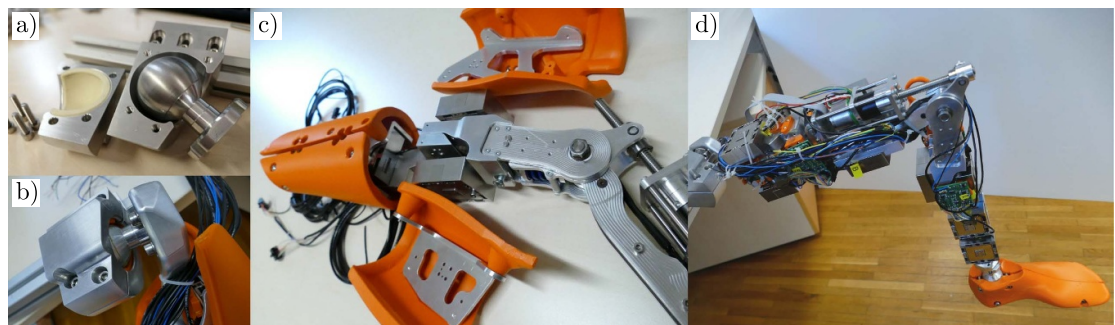


Figure 5. Construction details: (a) disassembled hip joint, (b) assembled hip joint, (c) disassembled surface shells, and (d) underlying leg structure with all the electronics.

straps. In such type of exoskeleton, two straps are normally located close to the knee joint to secure the alignment of the two rotation axes. The other two straps are usually placed distally from the joint for a better torque transmission (i.e. one strap close to the ankle and one closer to the hip). This arrangement has been adopted by the Exo-H3 exoskeleton (Technaid S.L., later shown in figure 7 right). In this configuration, each strap spans over two opposite surface shells, i.e. the front and back, which creates a force sensor pair. Such a force sensor pair detects compression forces of the straps and indicates their tightness. In a situation where an exoskeleton features a different arrangement of straps, i.e. two, three or more than four straps, it may happen that the forces are distributed over multiple surface shells and need to be summed up in the analysis.

Load cell orientations and the respective load capacities are shown in figure 4(b). Two different load capacities are used, a 200 N (K3D60a 200 N/VA) and a 500 N (K3D60a 500 N/VA) version. All sensors are oriented so that two load axes lie in the sagittal plane.

The K3D60a load cells are fairly large and therefore very resistant to eccentric loads. Eccentric forces result in torque loads that produce errors in the force measurement. These load cells produce a 1% error on the full scale for each 10 Nm of load (1%FS/10 Nm). A full load (500 N) acting on an exaggerated worst-case location (20 cm off-axis) would produce only a 1% error on the measurement scale. Application location of forces on the surface shell has thus a minimal effect on the quality of the signal. To further ensure the quality of the signal, the load cells are mounted securely according to the manufacturer's specifications.

A surface shell assembly joins three components. The first is an aluminum profile (light green component in figure 4(c)), which allows a rigid connection of the assembly to the force sensor. It acts both as a support and reinforcement for the plastic shell. ABS thermoplastic polymer and 3D additive manufacturing technology were used to create the surface shell (orange component in figure 4(c)). The combination of these two components creates a solid surface for the transfer of the interaction forces to the load cell. This rigidity ensures that there are no undesired contacts between components and that all the load is always transferred through the respective load cell. In addition, a small gap (5 mm) was also designed around all surface shells to prevent the contact between the shells or between the shells and the internal structure.

This assembly is a limited representation of the actual human skin properties, apart from the shape of the outer surface. However, the CAD model in figure 4(c) features an optional third component representing a layer of soft material that can be glued to the surface to emulate skin-like surface properties [44]. The development and validation of this human-like soft material will be a matter of future

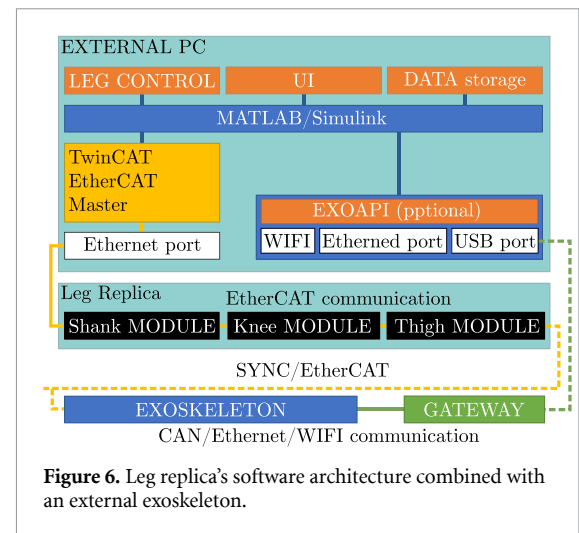


Figure 6. Leg replica's software architecture combined with an external exoskeleton.

improvements and is therefore not considered in this work. Figures 5(c) and (d) show the assembly and locations of the load cells and surface shells on the actual prototype.

The current leg replica allows for custom designs of the shells, e.g. bigger or smaller shell surface size, which may be needed by specific exoskeleton or end-user requirements. In this case, the structure of the leg replica design would remain unchanged, and only the shells would need to be substituted with the new ones.

3.4. Electronic system and software architecture

The hardware and software architecture of the leg replica is based on EtherCAT technology. Figure 6 represents the leg replica as three submodules connected by EtherCAT network to the main computer. The lower leg (shank) and upper-leg (thigh) modules represent the force sensors and respectively the hardware and software to acquire and process the sensor data. The SMARCOS motor also features some sensors and is part of the knee module. A Simulink (MathWorks, Inc.) user interface controls the leg replica and features the following advantages:

- It is an established solutions in the research environment, meaning that the users of the proposed leg replica will require minimal time to get familiar with the interface.
- It includes many tools to select, generate or tune different trajectories, as well as to read and log data visually and intuitively.
- If required, the user can change or build additional applications on top of the provided one.
- The ability to change the Simulink model of the leg replica will facilitate exoskeleton developers to test their exoskeletons without the need to change the exoskeleton software itself (for example, to store and process data in the same formats, send a specific trajectory, generate different perturbations, etc).

The software also addresses the problem of interfacing the exoskeleton with the leg replica, ensuring interoperability and data synchronization to allow developers test their exoskeletons with minimum effort. Considering that no communication standard exists specifically for exoskeleton applications, developers are normally using various communication protocols (USB, WIFI, CAN, EtherCAT, etc). As the leg replica prototype was developed to test various exoskeletons, the solution was to keep the exoskeleton and the leg replica as separate systems. The system allows data synchronization between the leg replica and other devices by providing both trigger input and output port connected by a Bayonet Neill–Concelman (BNC) connector to a port of the EtherCAT board.

As EtherCAT is the main communication protocol, developers can integrate the exoskeleton and the leg replica into the same architecture by connecting both systems to one master computer. As an option, manufacturers may use gateways and customized APIs to connect their exoskeletons to the same host computer and Simulink model. The proposed solution for data processing is to use MATLAB Simulink as it is able to record and process sensor data and also perform advanced controls for leg replication. The data is stored in independent files to allow researchers use their preferred tools to process data.

3.5. Forces, torques and inertia

This section describes the calculation of parameters used in the evaluation. Since the human leg density is unknown, the inertia of the human leg was simplified to a point mass inertia and calculated as follows:

$$I_{yy} = m_p L_m^2. \quad (1)$$

Here m_p is the mass point of the respective leg segment and the L_m the distance from the respective rotational joint. This way the data from tables 2 and 3 may be used to calculate it.

The load-cell measures and outputs the magnitudes of the X, Y, and Z axis. Different exoskeleton conditions are compared based on the resultant force. It is calculated as follows:

$$F_i = \sqrt{F_{i,x}^2 + F_{i,y}^2 + F_{i,z}^2}. \quad (2)$$

Here i corresponds to each of the eight load cells and x, y, z to the direction of the force.

The imposed torque of the orthosis on the knee joint is approximated using the Z axis components of all four lower leg load cells and their distances to the knee joint

$$T_o = r_1 F_{1,z} + r_3 F_{3,z} - r_2 F_{2,z} - r_4 F_{4,z}, \quad (3)$$

where r_1, r_2, r_3 and r_4 are the lengths of the lever to the knee axis and are equal to 0.305, 0.240, 0.145, and 0.125 m, respectively, according to the CAD design.

Parameters $F_{1,z}, F_{2,z}, F_{3,z}, F_{4,z}$ are the Z axis values from the respective load cells, as shown in figure 4(b).

Similarly, the tangential force acting on the lower leg is calculated using Y axis components as follows:

$$F_y = F_{1,y} + F_{2,y} + F_{3,y} + F_{4,y}, \quad (4)$$

where numbers 1 to 4 point to the respective load cell.

4. Experimental design

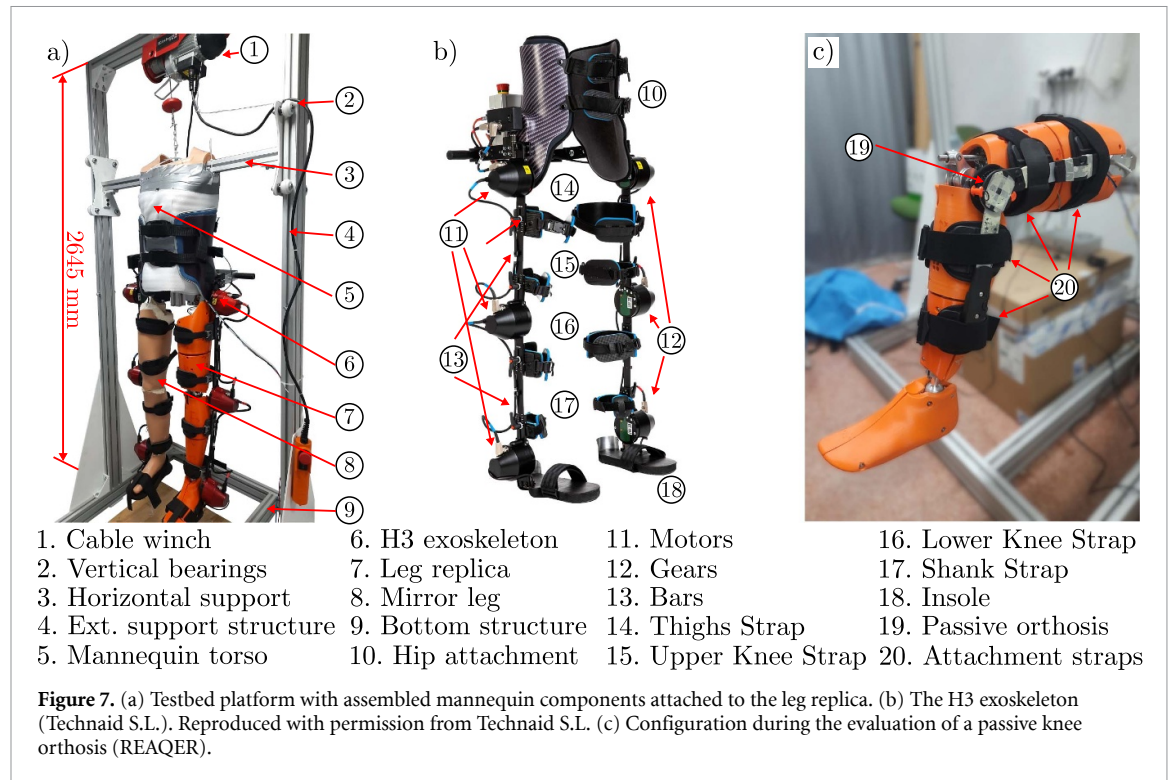
4.1. Exoskeleton testbed

A special testbed was designed to evaluate the leg replica and its capabilities to benchmark the physical interaction with an exoskeleton. The goal of this testbed was to simulate the use of wearable devices as close as possible to a real human user. The structure enables a proper wearing of full lower-limb devices, which usually require to be attached to the trunk.

The testbed, shown in figure 7(a), was built using a commercially available mannequin consisting of rigid bodies mimicking the anthropometric characteristics of the human torso and leg. The mannequin's left leg was replaced with our leg replica. The resulting dummy was attached to an external mechanical structure built using commercially available aluminum profiles. This structure helps to support the dummy in order to improve the control of the experimental process. The base of the support structure measures 1100 mm × 1100 mm and may be leveled and fixed to the floor for added stability. The whole structure has a height of 2645 mm and features two linear bearings that allow for the vertical movements of the dummy. A horizontal beam connects the two linear bearings and is attached to the torso of the mannequin, keeping it in the upright position. A cable winch is mounted on top for safe lifting.

The H3 exoskeleton, shown in figure 7(b), is a bilaterally powered exoskeleton with six active DoFs at the hip, knee and ankle joints. It features 10 pre-defined walking profiles, which can be run at different velocities. An on-board CAN interface serves as the main communication interface. The CAN interface is plugged in between the H3 and the control PC where communication is established using the Matlab's Vehicle Toolbox. 5 V trigger inputs and outputs allow synchronization with external devices.

The right leg ('mirror leg') of the mannequin was built from the original mannequin leg and split into an upper and lower leg and foot segments. To reinforce this mirror leg, wooden segments are inserted in the corresponding mannequin parts, filled and stabilized with expanding polyurethane foam. A 1-DoF hinge joint at the knee connects the upper and lower leg. A second hinge joint connects the lower leg segment with the foot. The segment lengths are consistent with the segment lengths of the leg replica. Similar to the leg replica, the mirror leg is connected to the torso assembly by a ball joint. Using the mirror leg,



the exoskeleton cuffs fit properly to the leg as if they were attached to a real human leg. Finally, the exoskeleton device was attached to the mannequin. The final mannequin assembly simulates full exoskeleton wearability, since the exoskeleton is attached both at the torso and the legs.

4.2. Experiment 1—actuation characterization

We conducted a first set of experiments to characterize the actuator dynamics. We fixed the leg replica through the hip joint to a horizontal aluminum profile at 60 cm from the ground. The upper leg was kept orthogonal to the profile and horizontal to the ground, whereas the lower leg was left free to move on the sagittal plane. The horizontal bar was fixed to a square base on the ground in order to prevent extra leg oscillations during the motion. The H3 exoskeleton actuators have a nominal joint velocity of 145 deg s^{-1} , a value that is lower than normative knee velocity during human walking, which spans from 370 deg s^{-1} when walking slowly (1.1 m s^{-1}) and 410 deg s^{-1} when walking fast (1.6 m s^{-1}), according to [45]. To avoid damaging the exoskeleton, we always maintained the leg replica velocity under such nominal threshold, while the exoskeleton was attached to the leg replica. Six sinusoidal amplitudes spacing the knee RoM from 10° to 60° were applied through a 60 s chirp signal and sent to the knee actuator. Chirp frequency was decreased with the tested RoM until the actuator was not able to follow the entire pattern for high frequency and high RoM. The data was then recorded and analyzed.

4.3. Experiment 2—interaction force estimation

A second set of experiments was conducted to evaluate the ability of the leg replica to measure changes in the coupling forces across different wearable devices and misalignment conditions.

4.3.1. Active exoskeleton—passive limb

The H3 exoskeleton was mounted on the mannequin and fixed to the leg replica and the mirror leg. Misalignments of the hip and knee joints were only considered in the vertical direction. Ankle misalignment was not examined. The leg's foot was correctly placed and tied in the foot's interface in all trials. The centers of rotation of the leg joints were easily recognizable. Their height from the ground were measured with a measuring tape. The same procedure was done by measuring the distance from the ground of the hip and knee actuator centers of H3 exoskeleton. The best aligned configuration was achieved by manually minimizing the displacement between the joints of leg replica and those of the exoskeleton. This configuration produced hip and knee misalignment of -0.5 cm and 0.6 cm respectively. Misalignment was defined as the difference between exoskeleton's joint height taken from the ground and the corresponding leg's joint height. The second configuration was tested by imposing a knee misalignment of -3.1 cm while the hip was kept at the same alignment of the previous configuration. In this way a first calibration check of the correct positioning of the exoskeleton on the mannequin was carried out. For each of the two alignment configurations, the entire mannequin wearing

the exoskeleton was lifted with the winch until the fully extended leg was at least 10 cm above the ground. Afterwards, the exoskeleton was set to perform a pre-defined human-like walking profile at gait speed of approximately 0.8 m s^{-1} for 180 s. Data acquisition for the leg replication was enabled from the Simulink control scheme. A start command on the Simulink interface was then sent to the exoskeleton to begin the defined motion. The test lasted 180 s, which allowed to record 37 walking cycles. For this test case, the resultant interaction force was compared for each load cells between the two conditions.

4.3.2. *Passive exoskeleton—active limb*

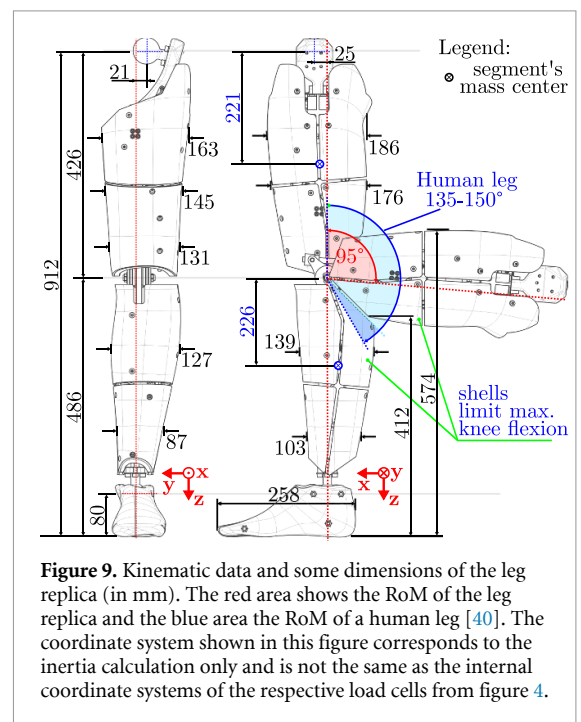
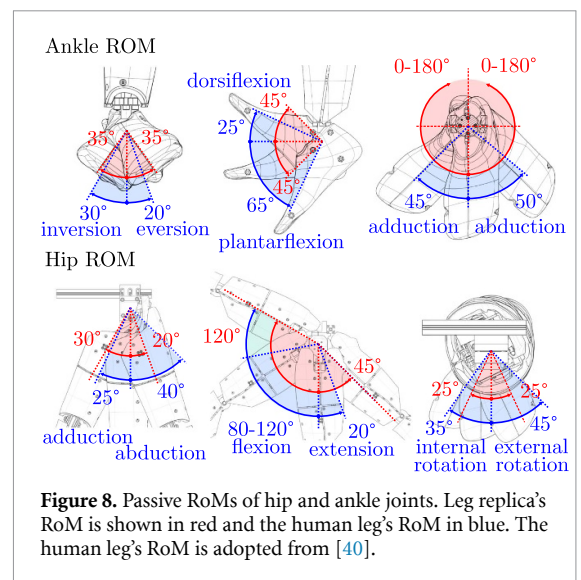
A further test was conducted by mounting a passive knee device while actuating the leg replica joint. For this test we selected a commercially available knee orthosis (REAQER knee orthosis) composed of two light aluminum frames connected by a hinge joint. Each frame has two connective cuffs for the fixation on the leg. Misalignments were only considered at the knee level and defined following the same procedure of the previous test. The orthosis was mounted on the leg replica while the mannequin was lifted from the ground. The reached configurations produced knee misalignment of -0.3 cm for the ‘best aligned’ configuration and -3.1 cm for the ‘misaligned’ configuration. A sinusoidal position trajectory from 5° (leg extended) to 65° (leg flexed) was imposed to the leg replica at a frequency of 0.2 Hz. The leg replica moved until 11 periods of the sinusoidal reference were completed. For this test case, the torque from the leg replica and the tangential forces recorded in the lower part of the leg were compared between the two conditions.

5. Results

5.1. Comparison to human leg properties

This section evaluates the leg replica's anthropometric properties in comparison to a human leg. The RoM of ankle and hip joint are depicted in figure 8. The leg replica RoM covers the full RoM of ankle inversion/eversion, ankle adduction/abduction and hip flexion/extension. As for the ankle plantarflexion/dorsiflexion, hip adduction/abduction and hip internal/external rotation, the leg replica covers a large portion of the human RoM, but not the full range. Nevertheless, the available RoM covers the RoM necessary for human walking [46].

As for knee joint, the RoM of the prototype is smaller than that of the human leg, as shown in figure 9, being the maximum flexion limited by the size of the two adjacent surface shells. In a human leg, soft muscles tissue may be compressed, allowing higher knee flexion. The leg replica's surface shells do not deform, thus limiting knee flexion to 95° , a value that has been chosen as a compromise between the RoM and the shell surface size. 95° is sufficient



for walking, according to Grimmer *et al* [45], who showed that maximum knee flexion during walking is 66° .

The replica’s joint-to-joint distances are not exactly the same as the mean value from the selected databases for a 50th percentile male. The reason is that the 3D surface scans were scaled to a hip height of 90.1 cm (dim. 83 in table 1). However, the length ratio of lower and upper leg segments was not changed during the scaling. According to [41], the heights of the leg joints in humans when standing are 7.3(0.6), 46.8(2.7) and 90.1(4.9) cm, for the ankle (dim. 59), knee (dim. 81), and hip (dim. 83), respectively. This is graphically depicted in figure 1(a). The leg replica’s CAD model was then referenced to the scaled CT scans and 3D scans, and not to the dimension

Table 5. Anthropometric data of human and prototype leg.

Parameter	Human mean(SD) Lower leg + Foot	CAD mean Lower leg + Foot	Human mean(SD) Upper leg	CAD mean Upper leg
I_{yy} (kgcm ²)	2109 (499) ^a	2820	2284 (702) ^a	4557
L (cm)	46.8 (2.7)	48.6	43.3 (5.6)	42.6
m_p (kg)	3.7 (0.7)	4.1	6.0 (1.2)	7.5
L_m (cm)	24.0 (2.1)	22.6	19.5 (3.2)	22.1
L_m (% L)	51.3 (3.5)	47	45.1 (4.4)	52
$m_{p,alu}$ (kg)	/	0.83	/	2.35
$m_{p,abs}$ (kg)	/	0.85	/	2.44

$m_{p,alu}$ and $m_{p,abs}$ are the respective leg segment's combined masses of the custom-made aluminum structure or plastic components. L is the respective leg segment length and L_m is the length from upper joint (knee or hip) to the segments (upper leg OR lower leg + foot) center of mass. L_m is represented in cm or in % of L .

^a The inertia standard deviation is calculated using the variance product for independent variables:

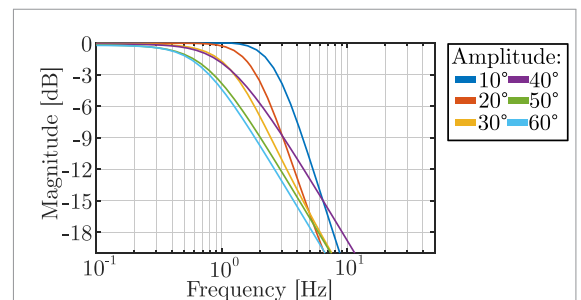
$$E(A \cdot B) = E(A) \cdot E(B); \text{Var}(A \cdot B) = E(A)^2 \cdot \text{Var}(B) + E(B)^2 \cdot \text{Var}(A) + \text{Var}(A) \cdot \text{Var}(B)$$

from table 1 directly. As seen in figure 9, the resulting sizes in the CAD model are 8.0, 48.6 and 91.2 cm for the ankle, knee and hip, respectively. All three values lie in the expected ranges of a human leg. The trochanterion and tibial height differences between CAD and real human leg is under one standard deviation. The difference in Popliteal height between CAD and real leg is slightly larger than one standard deviation.

Additionally, the leg replica's hip joint center is slightly tilted forward (25 mm) and slightly tilted sideways away from the center of the user's body (21 mm). This displacement agrees with that of a human leg [40] and human leg's CT scan. Figure 9 features additional dimensions of the leg for reference purposes.

The leg replica's dynamics are dictated by its mass and inertia. Figure 9 shows the location of the leg segment's mass centers. Table 5 collects the inertia properties based on equation (1) and dimensions from figure 9 and compares them to the inertia of a human leg. The corresponding leg masses and dimensions for the upper and lower leg and foot segments are summarized in tables 2 and 3. The mass properties of the leg replica are comparable to the properties of a human leg. Based on CAD values, the leg replica is slightly heavier than a human leg, where the 'lower leg and foot' complex is 0.4 kg heavier and the upper leg is 1.5 kg heavier. Consequently, the resulting inertia I_{yy} is also larger. The inertia estimation for the CAD 'lower leg and foot' complex is slightly larger, but still in acceptable range considering the human variability. The inertia estimation for the upper leg is larger than the human leg counterpart, even while considering the variability of the human leg.

The weight of aluminum components ($m_{p,alu}$) and the weight of plastic components ($m_{p,abs}$) were added to table 5 as additional information. The combined weight of the aluminum structure is 2.35 kg for the upper leg and 0.83 kg for the lower leg. Similarly, the plastic components weigh 0.85 kg for the 'lower leg and foot' complex and 2.44 kg for the upper leg.

**Figure 10.** Motor characterization performed at different amplitudes of the knee angle.

The rest of the mass is attributed to other standard components like force sensors, SMARCOS actuator, electronics, screws etc which cannot be modified. The complete physical leg replica weighs 10.6 kg, which is slightly less than the 11.6 kg estimated in the CAD model. This also means that the physical prototype weighs slightly more than a human leg, which weighs 9.7(1.5) kg, but is still in the range of human variability.

5.2. Analysis of experimental results

5.2.1. Actuation characterization

For the characterization test, the maximum frequency for each amplitude was chosen so that the motor could follow the trajectory until a frequency greater than the system bandwidth. A 4 Hz signal was applied for 10° of knee RoM, decreasing to 3 Hz for 20° and 2 Hz for 30°. RoM of 40°, 50° and 60° were only tested until 1.5 Hz of maximum frequency as their bandwidth was less than 1.5 Hz. Resulting bode plots are presented in figure 10, and cut-off frequencies are highlighted in table 6. The leg replica actuator was able to mimic a healthy gait profile in terms of velocity and range of motion up to an amplitude of approximately 47°. Considering the H3 as a device for rehabilitation tasks, the leg replica could reproduce the velocity limits of the exoskeleton. If a larger power to reach greater RoM at higher velocities would

Table 6. System bandwidth at different knee RoMs.

Amplitude (deg)	Bandwidth (Hz)	Ang. velocity (deg s ⁻¹)
10	2.58	928
20	1.91	687
30	1.27	458
40	1.23	441
50	0.90	324
60	0.74	266

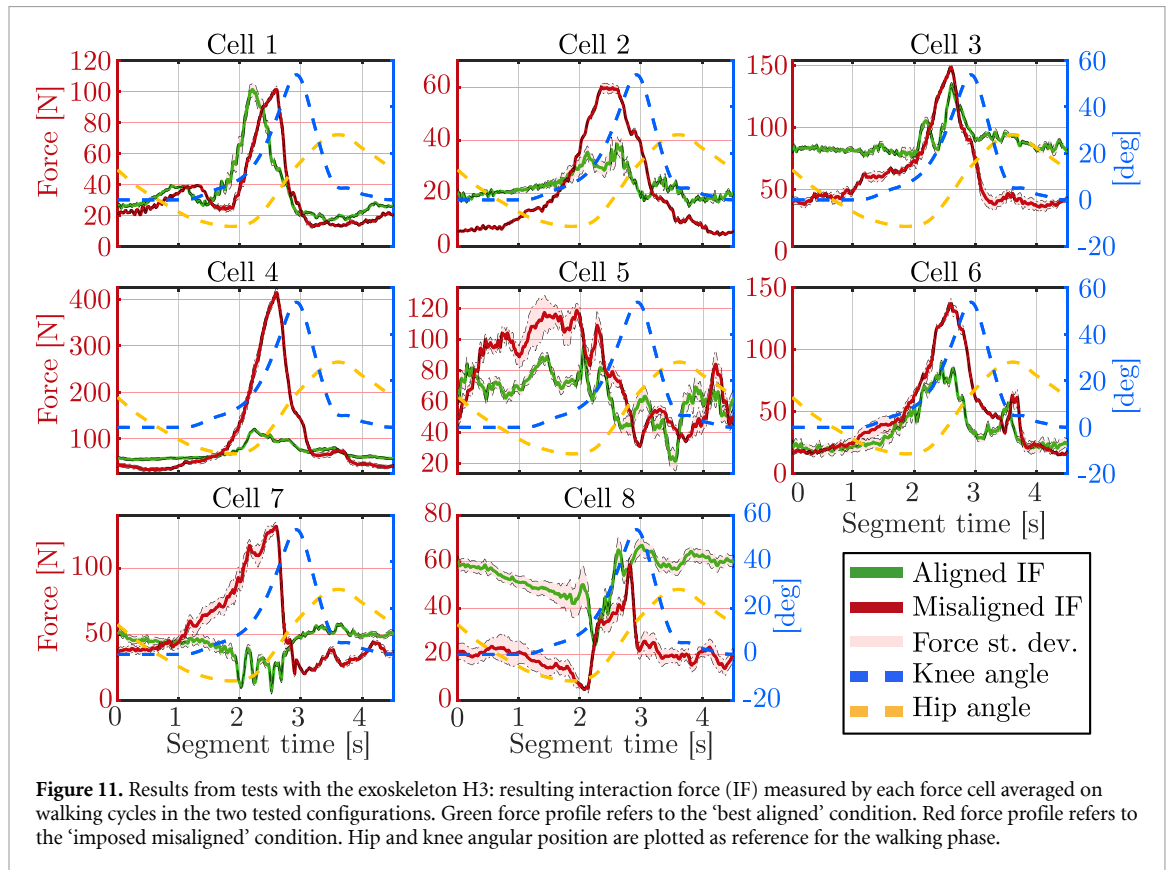


Figure 11. Results from tests with the exoskeleton H3: resulting interaction force (IF) measured by each force cell averaged on walking cycles in the two tested configurations. Green force profile refers to the ‘best aligned’ condition. Red force profile refers to the ‘imposed misaligned’ condition. Hip and knee angular position are plotted as reference for the walking phase.

be needed, the current SMARCOS actuator (70 W) shall be exchanged with a more powerful one. However, in the applications where the leg replica is meant to simulate a passive limb, no velocity limitations (in the range of human gait dynamics) would apply.

5.2.2. Interaction force estimation: active exoskeleton—passive limb

Figure 11 presents the magnitude of the resultant force of each cell in the case of active exoskeleton configuration. Force profiles are segmented on the cycles and presented together with standard deviation underlining their periodicity. Looking at figure 11, load cell’s 2, 4, 6 and 7 show the most drastic increase of forces in the misaligned case. Especially the force acting on the load cell number 4 increased several fold.

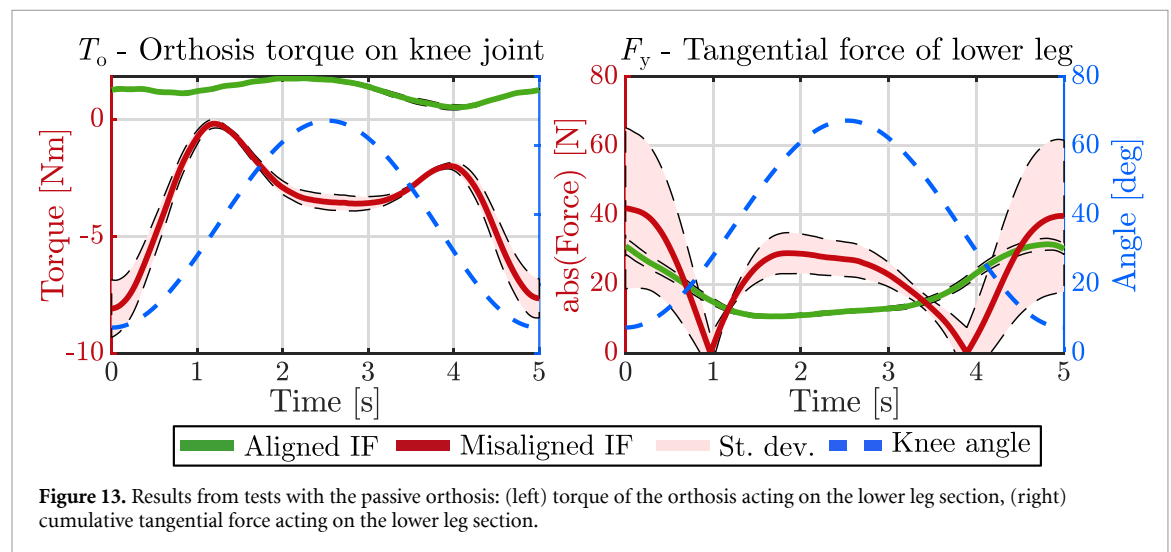
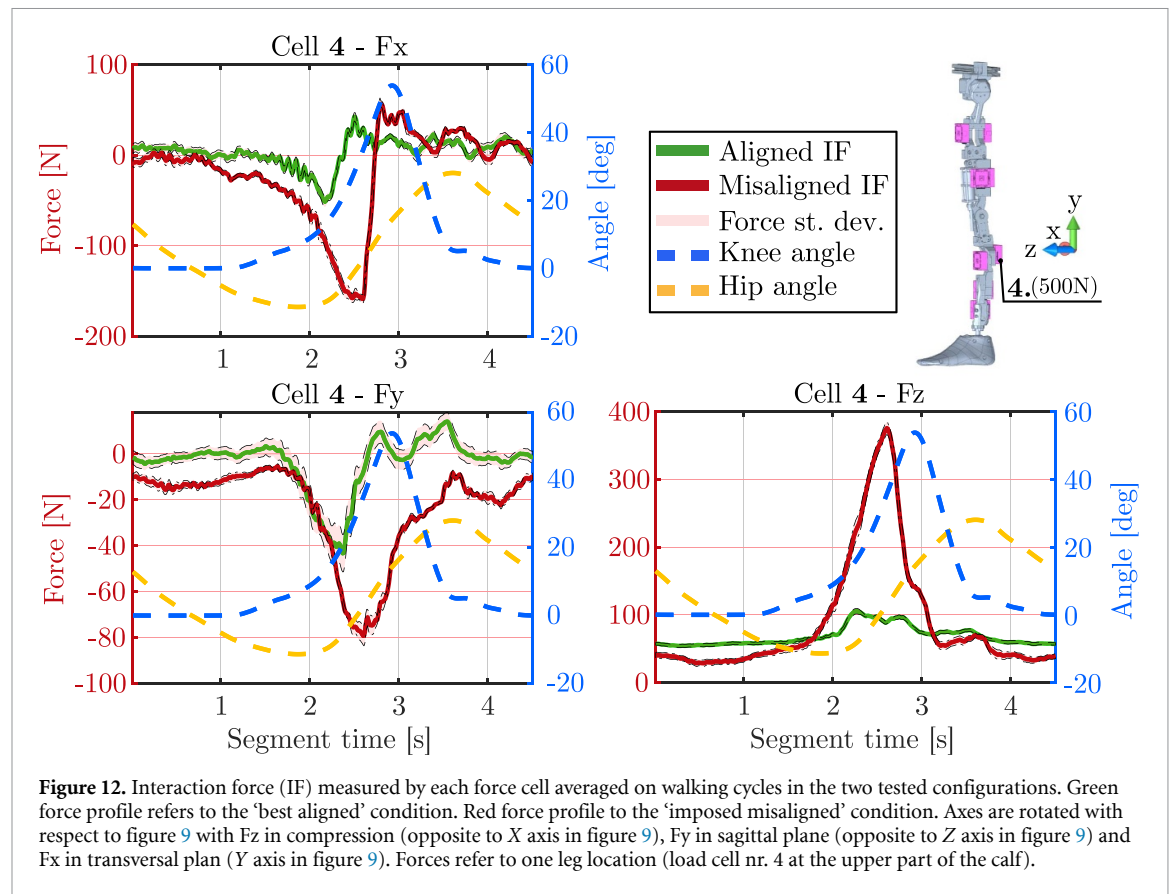
An example of data extracted from load cell number 4 is shown in figure 12, which shows the forces on the 3 axes. Cell 4 is positioned in the upper back part of the calf where forces are influenced both from

the hip and knee joint position. The analysis of cell 4 shows that the highest force component is in the Z axis. Although the X and Y axes also experience an increase in force magnitude, their increase is not as extreme as in the Z axis.

5.2.3. Interaction force estimation: passive exoskeleton—active limb

For the ‘passive device—active limb’ case, the torque imposed by the knee orthosis from equation (3) is compared in figure 13, which shows a higher torque when the device was not properly worn.

The passive orthosis is intended for stabilization and should not impose additional torque on the knee movement, meaning that the torque along the main rotation axis of the knee should be as small as possible. The same figure also presents the magnitude of tangential forces from equation (4) along the Y axis for the lower leg segment only (load cells number 1, 2, 3, 4), showing greater interaction and variability for the misaligned case.



6. Discussion

The main outcome of this paper is the construction of an active dummy leg based on human's leg anthropometric data, capable of sensing multi-directional interaction forces over its surface. At the time of writing this work, and to the best of our knowledge, no other devices with similar characteristics have been proposed for the study of pHEI. In the past, dummy legs used for wearable robot applications focused primarily on mimicking human

leg dimensions, without taking into account additional features such as realistic joint range of motion, human-like mass and inertia, or active joint actuation. The knee actuation system represents a novelty with respect to most of the work in the literature, since dummies are usually taken as passive platforms for robots to be worn. The joint actuation enables to test passive devices or scenarios where the human limb can still move or react to the robot (impedance control, transparent control, etc). In addition, none of the previous works focused on the transmission

of forces between the leg surface and the exoskeleton interface.

The force detection system embedded in the leg replica represents the main novelty with respect to the state-of-the-art. The force sensing systems present in most exoskeletons normally measure the overall interaction force at the joint level without providing information on how this interaction is distributed among the straps and in different directions. The number and position of the load cells beneath the leg replica surface allows the measurements of the interaction forces at different body sites. This enables the analysis of tangential force components independently from the overall interaction force. Furthermore, the combination of opposing surface shells allows measurement of the tightness or fastening force of exoskeleton straps, which is likely to play a crucial role in the comfort, safety, control, and efficiency perspectives. However, only few studies in the literature considered strap pretension when evaluating pHEI [12, 47].

Having the sensing system located beneath the surface and at different body sites eases the setup of the experimental system. pHEI is normally assessed by instrumenting the exoskeleton interfaces or joint with additional measuring devices. This additional instrumentation is placed between the exoskeleton interface and the surface of the leg and may therefore affect the measurements. Our testbed is able to wear a lower-limb exoskeleton without the need for additional sensing systems. This factor is particularly important when testing commercial devices, which normally offer limited access to their (force sensing) data.

This work has a series of limitations that will be a matter of future improvements. Currently, leg replica does not fully replicate the properties and features of human legs. For example, the range of motion of the knee is smaller than that of an actual human leg. Increasing the range of motion of the knee is possible but would require a redesign of the two shells located behind the knee joint. However, this modification would result in a smaller contact area and space for the attachment of exoskeleton straps. The weight of the leg replica prototype is close to that of a human leg, but further weight reductions are still possible. Custom-made aluminum parts and plastic housings are oversized and could be subject to weight reduction by improving their design.

The current set of human-like characteristics may enable the evaluation of wearable devices in terms of reachable motions and the capacity of actuators to overcome loads. Custom modifications to reduce or increase leg dimensions are not yet supported, that is, to change the length of leg segments. Therefore, at the moment only one single leg size is available. However, custom surface shells can be designed, i.e. thicker or thinner leg, and exchanged with the existing surface shells.

At the current state, this testbed cannot provide a proper safety evaluation of human-exoskeleton contact since (i) no pressure data are available and (ii) the real human-exoskeleton contact behavior might be considerably different to the one measured by our leg replica. The load cells in the leg replica record the overall interaction force on a specific shell, hiding the information on the real contact area and location at which the force has been applied to. Currently, no information on pressure is available, while studies conducting safety evaluations must address contact pressure to allow comparisons and evaluation of safety thresholds [48].

The rigid leg shells transfer the forces acting on the surface to the load cell placed beneath. However, their rigidity offers a poor description of the real human-exoskeleton contact. Comparative analyses are still feasible, such as the tests presented in this paper. Nevertheless, the lack of soft material to mimic skin and soft tissue of the human body raises questions on the validity of the recorded data when safety or other biological effects are investigated. One of the prioritized improvements concerns the replication of real human-exoskeleton contact dynamics by means of soft material around the leg replica mimicking human soft tissue characteristics. One possibility would be to design silicone shells with integrated force and pressure sensors, as suggested in [49].

In this work, we only explored the interaction of leg replica with an (active) exoskeleton and a (passive) orthosis, without studies involving human participants. The validation of the proposed leg replica using data from human experiments represents a mandatory step for the definition of the leg replica as a benchmarking tool. To this aim, the next efforts shall focus on building standard protocols for the contact evaluation in both dummies and humans. This will help define those conditions that can provide repeatable and reliable results from the leg replica, which will be comparable with those obtained in human tests. In the event of results below expectations, an iterative adaptation process will be performed until leg replica results can claim to be related with pHEI metrics in humans.

The preliminary tests conducted are not supposed to generate new scientific evidence on human pHRI. However, they confirm the general functioning of the proposed solution in terms of relative force contact evaluation. 3D forces were available in all the locations and the effect of a well performing device wearing are visible in the data recorded, especially at the normal forces (F_z) and the resulting force summation.

For the passive knee orthosis evaluation, our tests highlighted how misalignments could produce significant changes even in a lightweight passive device. The results focused on (i) the orthosis torque at the knee joint, as an indicator of the resistive effort imposed by the device on the active leg replica, and

(ii) the tangential forces of the leg experienced as consequence of the device tendency to move along the leg. This last indicator allows for future targeted tests, as shear forces play a key role in defining how well the motion is transferred between two bodies. In a proper user-exoskeleton interaction scenario, the tangential forces should be minimal, and only normal forces should act on a user. Additionally, higher magnitudes of shear forces reduce the amount of perpendicular force necessary for occlusion of blood vessels [50, 51]. A similar analysis with the active leg replica could be performed for the evaluation of active exoskeletons that implement transparent zero-torque control strategies.

In general, the potential of the leg replica for repeatable and systematic analysis was also demonstrated by the low standard deviation of the forces over cycles.

Further studies should carry out a more detailed and systematic analysis of the main influencing factors between interaction forces and motion. One typical application case concerns the evaluation of different misalignment compensation mechanisms and their ability to reduce undesired forces. This type of analysis would be better conducted in combination with accurate (e.g. optoelectronic) motion capture systems.

Another important discussion point is the degree of simplification of the leg replica joints. The introduction of an actuated knee represents an important novelty factor. It introduces the possibility to replicate typical knee trajectories and simulate spasticity in a patient, offering a wide range of possibilities for the evaluation of wearable knee devices. However, in contrast to the real human knee, in our leg replica the knee has only 1 DoF. This was due to the simplicity of the design and the existence of an operative actuation system (SMARCOS), capable of mimicking the actuation dynamics of human joints. To achieve a better kinematic representation of the knee, the entire actuation system should be replaced in the future. However, additional knee DoFs would substantially increase the mechanical complexity of the system as well as the knee joint encumbrance, and will introduce new requirements for the wearability of exoskeleton devices under examination.

Great advantages may be exploited by expanding the current leg design, including an actuation system for the hip and the ankle joints. The lack of actuation in these joints limits the potential for leg replica as a testing device for full lower leg exoskeleton devices. An active hip joint would enable a more accurate reproduction of typical motions such as walking and sit-to-stand. An active ankle would allow evaluations of ankle exoskeleton joints, which are often approximated as passive joints in current leg exoskeleton realizations.

So far, the lack of actuation in many joints limits the replication of realistic rehabilitation scenarios.

However, thanks to the backdrivability of the knee actuator, the behavior of the tetraplegic patient can be simulated. Other conditions, such as hemiplegic, would be difficult to properly represent with the given actuation system. However, our leg replica represents a compact and robust tool that, in spite of the listed limitations, finds application in several experimental scenarios for pHEI evaluation. Its functioning and adaptability under controlled conditions allow one to carry out a set of reproducible experiments useful for the study of pHEI and its influencing factors.

The presented test platform is a unique tool to address the pressing need for more comprehensive exoskeleton benchmarking solutions. Although standards from international committees (e.g. ASTM F48, ISOTC299, and CEN/CENELEC) have produced valuable work in the direction of standardizing testing methods on exoskeleton performance, the wearable robot community still requires harmonization in terms of reproducible protocols, testbeds, set of metrics and data format [52]. The presented solution, together with data-driven evidence, has the possibility of producing new knowledge in the field of pHEI, complementing the efforts done so far on the functional evaluation side [53].

7. Conclusion

We presented the design and construction of a robotic leg replica with an integrated sensory system that enables measurements of interaction forces between an exoskeleton and a leg. The prototype has human-like properties in terms of inertia, range of motion and velocity, and features a compliant active knee joint powered by the SMARCOS actuator.

The leg was tested in two scenarios to demonstrate its ability to act as a passive and active sensing device. In the first case, the commercially available H3 lower limb exoskeleton from Technaid was worn on a full-body dummy, where one leg was replaced with the replica leg. In the second case, the leg replica wore a passive leg orthosis/brace. In both cases, the replica detected higher loads when the two devices were not properly worn (i.e. in the presence of imposed joint misalignments). Additionally, we observed that the standard deviation across measurement cycles in the aligned scenarios was low, which shows the good potential of the device to perform reproducible experiments. The leg replica in its current version can be used to compare different exoskeleton solutions, e.g. to test different hardware or control designs and their ability to adapt to a human leg. One of the main future directions will be to prove the ability of the leg replica to represent real interactions between humans and exoskeletons. To this aim, future prototype iterations will aim to more closely mimic the motions of human joints, to include human-like soft tissues, and to reproduce different limb sizes, morphology, or mass. This represents a necessary step

before comparing the results with human-oriented tests and the examination of leg potential as a real benchmarking device.

Data availability statement

Part of the data is still relevant for future publications. The authors would like to reserve the right to choose whether and when to make them available on request. The data that support the findings of this study are available upon reasonable request from the authors.

Acknowledgments

This work was supported by the project EXOSAFE, awarded by the COVR European Project under Grant Agreement No. 779966. The authors would like to thank Andrej Trošt for his contribution in the design and assembly of the leg replica electronics. The authors would also like to thank Dirk Lefeber for all assistance and discussions in the project.


ORCID iDs

Miha Dežman  <https://orcid.org/0000-0001-7160-749X>


Stefano Massardi  <https://orcid.org/0000-0002-7260-663X>

David Pinto-Fernandez  <https://orcid.org/0000-0003-0139-1261>

Victor Grosu  <https://orcid.org/0000-0002-3386-0811>

Carlos Rodriguez-Guerrero  <https://orcid.org/0000-0002-0297-9748>

Jan Babič  <https://orcid.org/0000-0002-1870-8264>

Diego Torricelli  <https://orcid.org/0000-0001-8767-3395>

References

- [1] Young A J and Ferris D P 2016 State of the art and future directions for lower limb robotic exoskeletons *IEEE Trans. Neural Syst. Rehabil. Eng.* **25** 171–82
- [2] Jørgensen L, Jacobsen B K, Wilsaard T and Magnus J H 2000 Walking after stroke: does it matter? Changes in bone mineral density within the first 12 months after stroke. A longitudinal study *Osteoporosis Int.* **11** 381–7
- [3] Awad L N, Esquenazi A, Francisco G E, Nolan K J and Jayaraman A 2020 The ReWalk Restore™ soft robotic exosuit: a multi-site clinical trial of the safety, reliability and feasibility of exosuit-augmented post-stroke gait rehabilitation *J. NeuroEng. Rehabil.* **17** 1–11
- [4] Pedro Pinho J, Taira C, Parik-Americano P, Suplino L O, Bartholomeu V P, Hartmann V N, Umemura G S and Forner-Cordero A 2020 A comparison between three commercially available exoskeletons in the automotive industry: an electromyographic pilot study *2020 8th IEEE RAS/EMBS Int. Conf. for Biomedical Robotics and Biomechatronics (BioRob)* (IEEE) pp 246–51
- [5] O'Sullivan L, Nugent R and van der Vorm J 2015 Standards for the safety of exoskeletons used by industrial workers performing manual handling activities: a contribution from the robo-mate project to their future development *Proc. Manuf.* **3** 1418–25
- [6] Farris D J, Harris D J, Rice H M, Campbell J, Weare A, Risius D, Armstrong N and Rayson M P 2022 A systematic literature review of evidence for the use of assistive exoskeletons in defence and security use cases *Ergonomics* **63** 1–27
- [7] Jhawar V 2018 Design of a knee exoskeleton for gait assistance *PhD Thesis Arizona State University*
- [8] Pons J L 2008 *Wearable Robots: Biomechatronic Exoskeletons* (New York: Wiley)
- [9] Cherry M S, Kota S, Young A and Ferris D P 2016 Running with an elastic lower limb exoskeleton *J. Appl. Biomech.* **32** 269–77
- [10] Asbeck A T, De Rossi S M M, Holt K G and Walsh C J 2015 A biologically inspired soft exosuit for walking assistance *Int. J. Robot. Res.* **34** 744–62
- [11] Massardi S, Rodriguez-Cianca D, Pinto-Fernandez D, Moreno J C, Lancini M and Torricelli D 2022 Characterization and evaluation of human–exoskeleton interaction dynamics: a review *Sensors* **22** 3993
- [12] Schiele A and Van der Helm F C T 2009 Influence of attachment pressure and kinematic configuration on pHRI with wearable robots *Appl. Bionics Biomech.* **6** 157–73
- [13] Stienen A H A, Hekman E E G, Van Der Helm F C T and Van Der Kooij H 2009 Self-aligning exoskeleton axes through decoupling of joint rotations and translations *IEEE Trans. Robot.* **25** 628–33
- [14] Quinlivan B, Asbeck A, Wagner D, Ranzani T, Russo S and Walsh C 2015 Force transfer characterization of a soft exosuit for gait assistance *Int. Design Engineering Technical Conferences and Computers and Information in Engineering Conf.* vol 57120 (American Society of Mechanical Engineers) p V05AT08A049
- [15] Tamez-Duque Jus, Cobian-Ugalde R, Kilicarslan A, Venkatakrishnan A, Soto R and Luis Contreras-Vidal J 2015 Real-time strap pressure sensor system for powered exoskeletons *Sensors* **15** 4550–63
- [16] Fosch Villaronga E 2016 ISO 13482:2014 and its confusing categories. Building a bridge between law and robotics *New Trends in Medical and Service Robots* (Berlin: Springer) pp 31–44
- [17] Massardi S, Pinto-Fernandez D, Veneman J F and Torricelli D 2020 Testing safety of lower limbs exoskeletons: current regulatory gaps *Int. Symp. on Wearable Robotics* (Berlin: Springer) pp 145–9
- [18] Bessler J, Prange-Lasonder G B, Schulte R V, Schaake L, Prinsen E C and Buurke J H 2020 Occurrence and type of adverse events during the use of stationary gait robots—a systematic literature review *Front. Robot. AI* **7** 158
- [19] Portela M A, Zapata S, Arango C C, Pérez V Z and Betancur M J 2017 Evaluation plan of a mechatronic system for anterior cruciate ligament rehabilitation *2017 IEEE 3rd Colombian Conf. on Automatic Control (CCAC)* (IEEE) pp 1–6
- [20] Bostelman R and Hong T et al 2018 Test methods for exoskeletons—lessons learned from industrial and response robotics *Wearable Exoskeleton Syst. Des. Control Appl* **13** 335–61
- [21] Noda T, Teramae T, Ugurlu B and Morimoto J 2014 Development of an upper limb exoskeleton powered via pneumatic electric hybrid actuators with bowden cable *2014 IEEE/RSJ Int. Conf. on Intelligent Robots and Systems (IEEE)* pp 3573–8
- [22] Ashrafiun H, Grosh K, Burke K J and Bommer K 2010 An intelligent exoskeleton for lower limb rehabilitation *Int. Design Engineering Technical Conf. and Computers and Information in Engineering Conf.* vol 44106 pp 3–9
- [23] Madani T, Daachi B and Djouani K 2016 Non-singular terminal sliding mode controller: application to an actuated exoskeleton *Mechatronics* **33** 136–45
- [24] Dávila-Vilchis J-M, Ávilas L A Z, Ávila Vilchis J C and Vilchis-González A H 2019 Design methodology for soft wearable devices—the MOSAR case *Appl. Sci.* **9** 4727

- [25] Baser O, Kizilhan H and Kilic E 2016 Mechanical design of a biomimetic compliant lower limb exoskeleton (biocomex) *2016 Int. Conf. on Autonomous Robot Systems and Competitions (ICARSC)* (IEEE) pp 60–65
- [26] Ito T, Ayusawa K, Yoshida E and Kobayashi H 2020 Simultaneous control framework for humanoid tracking human movement with interacting wearable assistive device *IEEE Robot. Autom. Lett.* **5** 3604–11
- [27] Kaneko K, Kanehiro F, Morisawa M, Miura K, Nakaoka S'ichiro and Kajita S 2009 Cybernetic human hrp-4c *2009 9th IEEE-RAS Int. Conf. on Humanoid Robots* (IEEE) pp 7–14
- [28] Akiyama Y, Yamada Y, Ito K, Oda S, Okamoto S and Hara S 2012 Test method for contact safety assessment of a wearable robot-analysis of load caused by a misalignment of the knee joint *2012 IEEE RO-MAN: The 21st IEEE Int. Symp. on Robot and Human Interactive Communication* (IEEE) pp 539–44
- [29] Bessler-Etten J, Schaake L, Prange-Lasonder G B and Buurke J H 2022 Assessing effects of exoskeleton misalignment on knee joint load during swing using an instrumented leg simulator *J. NeuroEng. Rehabil.* **19** 1–18
- [30] Wan X, Liu Y, Akiyama Y and Yamada Y 2020 Monitoring contact behavior during assisted walking with a lower limb exoskeleton *IEEE Trans. Neural Syst. Rehabil. Eng.* **28** 869–77
- [31] Georgarakis A-M, Stämpfli R, Wolf P, Riener R and Duarte J E 2018 A method for quantifying interaction forces in wearable robots *2018 7th IEEE Int. Conf. on Biomedical Robotics and Biomechanics (Biorob)* (IEEE) pp 789–94
- [32] Akiyama Y, Yamada Y and Okamoto S 2015 Interaction forces beneath cuffs of physical assistant robots and their motion-based estimation *Adv. Robot.* **29** 1315–29
- [33] Akiyama Y, Okamoto S, Yamada Y and Ishiguro K 2015 Measurement of contact behavior including slippage of cuff when using wearable physical assistant robot *IEEE Trans. Neural Syst. Rehabil. Eng.* **24** 784–93
- [34] Rathore A, Wilcox M, Zuleima Morgado Ramirez D, Loureiro R and Carlson T 2016 Quantifying the human-robot interaction forces between a lower limb exoskeleton and healthy users *2016 38th Annual Int. Conf. IEEE Engineering in Medicine and Biology Society (EMBC)* (IEEE) pp 586–9
- [35] Levesque L, Pardoel S, Lovrenovic Z and Doumit M 2017 Experimental comfort assessment of an active exoskeleton interface *2017 IEEE Int. Symp. on Robotics and Intelligent Sensors (IRIS)* (IEEE) pp 38–43
- [36] Wang Y, Qiu J, Cheng H and Zheng X 2020 Analysis of human-exoskeleton system interaction for ergonomic design *Hum. Factors* **0018720820913789**
- [37] Leal-Junior A, Theodosiou A, Díaz C, Marques C, José Pontes M, Kalli K and Frizera-Neto A 2018 Fiber Bragg gratings in CYTOP fibers embedded in a 3D-printed flexible support for assessment of human-robot interaction forces *Materials* **11** 2305
- [38] Leal-Junior A G, Diaz C R, Jose Pontes M J, Marques C and Frizera A 2019 Polymer optical fiber-embedded, 3D-printed instrumented support for microclimate and human-robot interaction forces assessment *Opt. Laser Technol.* **112** 323–31
- [39] Clauser C E, McConville J T and Young J W 1969 Weight, volume, and center of mass of segments of the human body AMRL-TR-69-70, NASA-CR-112672 (Aerospace Medical Research Laboratory, Aerospace Medical Division, Air Force Systems Command, Wright-Patterson Air Force Base, Ohio)
- [40] Neumann D A 2016 *Kinesiology of the Musculoskeletal System-E-Book: Foundations For Rehabilitation* (Missouri: Elsevier)
- [41] Gordon C C et al 2014 *Anthropometric survey of U.S. army personnel: methods and summary statistics* Technical Report NATICK/TR-15/007 (U.S. Army Natick Soldier Research Development and Engineering Center)
- [42] Ducastel V, Langlois K, Rossini M, Grosu V, Vanderborcht B, Lefebvre D, Verstraten T and Geeroms J 2021 Smarcos: off-the-shelf smart compliant actuators for human-robot applications *Actuators* **10** 289
- [43] Van Ham R, Vanderborcht B, Van Damme Mel, Verrelst Born and Lefebvre D 2007 Maccopa, the mechanically adjustable compliance and controllable equilibrium position actuator: design and implementation in a biped robot *Robot. Auton. Syst.* **55** 761–8
- [44] Dabrowska A K, Rotaru G-M, Derler S, Spano F, Camenzind M, Annaheim S, Stämpfli R, Schmid M and Rossi R M 2016 Materials used to simulate physical properties of human skin *Skin Res. Technol.* **22** 3–14
- [45] Grimmer M, Elshamshory A A and Beckerle P 2020 Human lower limb joint biomechanics in daily life activities: a literature based requirement analysis for anthropomorphic robot design *Front. Robot. AI* **7** 13
- [46] Mentiplay B F, Banky M, Clark R A, Kahn M B and Williams G 2018 Lower limb angular velocity during walking at various speeds *Gait Posture* **65** 190–6
- [47] Langlois K, Rodriguez-Cianca D, Serrien B, De Winter J, Verstraten T, Rodriguez-Guerrero C, Vanderborcht B and Lefebvre D 2020 Investigating the effects of strapping pressure on human-robot interface dynamics using a soft robotic cuff *IEEE Trans. Med. Robot. Bionics* **3** 146–55
- [48] Kermavnar T, O'Sullivan K J, de Eyto A and O'Sullivan L W 2021 Relationship between interface pressures and pneumatic cuff inflation pressure at different assessment sites of the lower limb to aid soft exoskeleton design *Hum. Factors* **63** 1061–75
- [49] Teyssier M, Parilusyan B, Roudaut A and Steimle Jurgen 2021 Human-like artificial skin sensor for physical human-robot interaction *2021 IEEE Int. Conf. on Robotics and Automation (ICRA)* (IEEE) pp 3626–33
- [50] Lachenbruch C, Tzen Y-T, Brienza D M, Karg P E and Anthony Lachenbruch P 2013 The relative contributions of interface pressure, shear stress and temperature on tissue ischemia: a cross-sectional pilot study *Ostomy Wound Manage.* **59** 25–34
- [51] Goossens R H M, Zegers R, van Dijke G A H and Snijders C J 1994 Influence of shear on skin oxygen tension *Clin. Physiol.* **14** 111–8
- [52] Babič J, Laffranchi M, Tessari F, Verstraten T, Novak D, Šarabon N, Ugurlu B, Peternel L, Torricelli D and Veneman J F 2021 Challenges and solutions for application and wider adoption of wearable robots *Wearable Technol.* **2** e14
- [53] Torricelli D and Pons J L 2019 Eurobench: preparing robots for the real world *Wearable Robotics: Challenges and Trends: Proc. 4th Int. Symp. on Wearable Robotics, WeRob2018 (Pisa, Italy, 16–20 October 2018)* vol 3 (Springer) pp 375–8